PHYSICAL REVIEW B **93**, 035311 (2016)

Anisotropy of electron and hole *g* tensors of quantum dots: An intuitive picture based on spin-correlated orbital currents

J. van Bree,[1,2,*] A. Yu. Silov,[1] M. L. van Maasakkers,[1] C. E. Pryor,[2] M. E. Flatté,[1,2,†] and P. M. Koenraad[1]

[1]*PSN, COBRA, University of Technology Eindhoven, 5600 MB Eindhoven, The Netherlands*

[2]*Department of Physics and Astronomy and Optical Science and Technology Center, University of Iowa, Iowa City, Iowa 52242, USA*

(Received 23 September 2015; published 25 January 2016)

Using single spins in semiconductor quantum dots as qubits requires full control over the spin state. As the *g* tensor provides the coupling in a Hamiltonian between a spin and an external magnetic field, a deeper understanding of the *g* tensor underlies magnetic-field control of the spin. The *g* tensor is affected by the presence of spin-correlated orbital currents, of which the spatial structure has been recently clarified. Here we extend that framework to investigate the influence of the shape of quantum dots on the anisotropy of the electron *g* tensor. We find that the spin-correlated orbital currents form a simple current loop perpendicular to the magnetic moment's orientation. The current loop is therefore directly sensitive to the shape of the nanostructure: for cylindrical quantum dots, the electron *g*-tensor anisotropy is mainly governed by the aspect ratio of the dots. Through a systematic experimental study of the size dependence of the separate electron and hole *g* tensors of InAs/InP quantum dots, we have validated this picture. Moreover, we find that through size engineering it is possible to independently change the sign of the in-plane and growth direction electron *g* factors. The hole *g* tensor is found to be strongly anisotropic and very sensitive to the radius and elongation. The comparable importance of itinerant and localized currents to the hole *g* tensor complicates the analysis relative to the electron *g* tensor.

DOI: 10.1103/PhysRevB.93.035311

I. INTRODUCTION

The *g* tensor describes the fundamental coupling between a spin and an external magnetic field, and therefore it plays an essential role in the physics of spins. Manipulation of this tensor, for example by an electric field, allows for an effective control over the spin even when an externally applied magnetic field is static. This proves to be advantageous for the local addressing of spins [1,2], tilting the spin's precessional axis [3–7], or high-speed spin manipulation [8]. Of particular interest is the *g* tensor of carriers in (self-assembled) semiconductor quantum dots, as a single spin inside these nanostructures is a promising candidate for forming a solid-state qubit [9,10]. Although the electric-field sensitivity of the *g* tensor can be exploited as a means to control the spin, it can also generate decoherence when electrical (charge) noise is present [11]. For optimal performance, control over the absolute value, sign, and anisotropy of the *g* tensor is crucial. The effects of quantum confinement and strain of the quantum dot are usually captured by a parametrization of the *g* tensor in terms of size, shape, and composition [12–17]. A better understanding of the origin of the *g* tensor is therefore helpful in the further exploration of electrical spin control.

The *g* tensor describes effectively how spin-orbit interaction modifies the magnetic moment of a carrier. In general, the magnetic moment of a carrier can have contributions from its spin and orbital degrees of freedom. In the solid state, the presence of spin-orbit interaction and coupling between bands leads to a spin-correlated orbital moment [18]. We will refer to this as just the orbital moment in this article, noting that we mean the spin-dependent orbital moment and not the conventional orbital moment in the absence of spin-orbit interaction. For a conduction-band electron in narrow-gap III-V semiconductors, the orbital moment can be much larger than the spin moment itself; the magnetic response of the electron ground-state spin is therefore dominated by the orbital moment [18]. These orbital moments are generated through orbital currents, of which the spatial structure in nanostructures has been recently investigated [19]. The dominant current was found to circulate within the nanostructure. It vanishes at the edge and center, and it peaks about midway between. This resembles a current loop, and this intuitive physical picture is capable of explaining the size and composition dependence of the spin-correlated orbital moment in various systems [20]. Although the shape of the nanostructure has been predicted to be influential on the electron *g* tensor [12,13], an intuitive picture of this relation is still lacking. In Sec. II of this article, we will show, using numerical $\mathbf{k}\cdot\mathbf{p}$ calculations and the intuitive framework of orbital currents, how the anisotropy of the electron *g* tensor is linked to the shape of a nanostructure.

Experimental efforts have been made to characterize the *g* factors (i.e., components of the *g* tensor) of excitons [21–26], and of individual electron and holes [27–36] confined in quantum dots. Also, electric control over *g* factors has been shown [25,29,33,35–37]; in particular, it was found that the hole *g* factor is much more sensitive to an electric field than the electron *g* factor. As quantum confinement and strain affect the *g* tensor, it is generally found that the inhomogeneous distribution of quantum dots leads to different *g* factors and electric-field sensitivities for each individually measured quantum dot. Although there are numerous reports of electron or hole *g*-factor measurements on individual quantum dots, there are only limited systematic reports on the size dependence of the *g* factors [22–25]. Moreover, these only involve the exciton *g* factor in a particular direction, and therefore they do not reveal the size dependence of the separate electron and hole *g* tensors and their anisotropies.

*j.v.bree@tue.nl

†michael_flatte@mailaps.org

In Sec. III, we report a systematic experimental study of the size dependence of the separate electron and hole g factors of InAs/InP quantum dots in both the growth and in-plane directions. It provides insight into the possibility to size-engineer the magnitude and sign of components of the g tensor. Moreover, it allows us to verify the correlation motivated by the theory in Sec. II between the nanostructure's shape and the anisotropy of the electron g tensor. We have measured the separate electron and hole g tensors using angle-dependent magnetoluminescence (Sec. III A). Contrary to what has been found before [30,31,35,36], we have systematically measured a strong electron g-factor anisotropy (Sec. III B). Through the systematic study of the size dependence, we have been able to understand this behavior, and we find it to be in good agreement with our theoretical predictions. The experimentally measured hole g factors (Sec. III C) agree well with numerical calculations. Also, the exciton diamagnetic coefficients (Sec. III D) are found to be anisotropic; analogous to the electron g tensor, this anisotropy can be correlated with the shape of the quantum dots.

II. THEORY OF SPIN-CORRELATED ORBITAL MOMENTS IN ANISOTROPIC DOTS

Calculations using analytical perturbation theory [12] and numerical methods [13] have predicted that the shape of the nanostructure influences the anisotropy of the electron g tensor. However, an intuitive explanation of this relation is lacking. We therefore investigate how the orbital currents change when the spin of a carrier is oriented in different directions. Intuitively, one would expect the orbital current to circulate in a plane perpendicular to the orbital moment. To verify this intuition, we calculate explicitly the orbital current density of cylindrical InAs/InP quantum dots.

We compute the electron ground state using strain-dependent eight-band $\mathbf{k}\cdot\mathbf{p}$ theory in the envelope approximation with finite differences on a real-space grid [38–40]. The strain is calculated using linear elasticity continuum theory. The calculations are performed at $T = 0$ K and material parameters are taken from Ref. [41]. The magnetic field is included by coupling it to both the spin part (using the Zeeman Hamiltonian) and the orbital part (using the gauge invariance) of the wave function [13,14]. Using a small magnetic field of 0.1 T, the electron ground state's magnetic moment is oriented an angle η away from the symmetry z axis of the quantum dot toward the in-plane x axis.

Knowing the real-space wave function of this oriented electron ground state, we can calculate the orbital current using the formalism developed in Ref. [19]. We use an envelope-function formalism to describe the electronic state, where the wave function is the sum of products of a (slowly varying) envelope function and a (quickly varying) Bloch function. When evaluating the spatial dependence of the current associated with that state, we evaluate the current operator, which is directly related to the spatial derivative operator. As a result, the derivative of the Bloch function dominates the current [19]. The orbital current can be generally decomposed into localized currents, which are restricted to a unit cell, and itinerant currents, which are distributed throughout the quantum dot. Since the electron ground state consists mainly of conduction-band states that carry no Bloch orbital moment, the localized currents have a negligible contribution to the total current. The dominant contribution to the orbital current comes, therefore, from the itinerant currents related to the Bloch velocity. For more details, see Refs. [19,20].

In Fig. 1(a), we show selected streamlines of this dominant orbital current density for three differently sized quantum dots at three different values of η. We confirm the previous finding that the current is zero at the center and edge of the quantum dot, and it peaks somewhere in between. We also observe that for $\eta \neq 0^\circ$, the current density is not uniform along a streamline, which originates from the divergence-free nature of the current density. More importantly, however, we indeed observe that the current circulates in a plane perpendicular to the magnetic moment. The orbital moment is thus generated from a current loop perpendicular to its orientation.

This finding has an interesting consequence. The magnitude of an orbital moment μ_{orb} depends on the area A encircled by the integrated current I, $\mu_{\mathrm{orb}} = IA$. The orbital moment is therefore sensitive to the shape of the quantum dot through the area encircled by its generating current. In particular, we expect for cylindrically shaped quantum dots with radius R and height H,

$$\mu^z_{\mathrm{orb}} \propto R^2, \quad \mu^x_{\mathrm{orb}} \propto \frac{1}{2}RH = \frac{R^2}{\lambda},$$

where we used the aspect ratio $\lambda = 2R/H$.

We find indeed that the orbital moment follows this expectation; see Fig. 1(b). The orbital moment of the quantum dot with a near-unity aspect ratio is isotropic, while for large (small) aspect ratios we observe that μ^x_{orb} is smaller (larger) than μ^z_{orb}. We point out that the anisotropy has significant magnitude; in this example, it is $>15\%$ of the orbital moment itself. Only orbital currents that are distributed throughout the quantum dot will sense the shape of the nanostructure. Other contributions [19] to the total magnetic moment (notably the spin moment) arise mostly from small localized currents, and indeed they do not exhibit a significant anisotropy; see Fig. 1(b). The orbital moment also depends, through the integrated current I, on the geometry of the nanostructure.

To investigate whether the anisotropy is truly governed by the shape of the quantum dot, we show in Fig. 1(c) how the anisotropy depends on the aspect ratio and the confinement energy. The strong dependence on the aspect ratio indicates directly that the anisotropy is driven by the nanostructure's shape. Simultaneously, we observe only a weak dependence of the anisotropy on the confinement energy. For a fixed aspect ratio, we expect the confinement energy to depend only on the volume, and we therefore infer that the anisotropy is relatively insensitive to the overall size of the nanostructure. This relation is also showcased by the three quantum dots exemplified in Figs. 1(a) and 1(b): they have nearly the same confinement energy yet very different orbital moment anisotropies.

III. EXPERIMENTAL RESULTS

To experimentally verify whether the orbital moment anisotropy is indeed linked to the shape of nanostructures, we have measured the g tensor of individual InAs/InP quantum dots. We have studied these quantum dots in the past, and

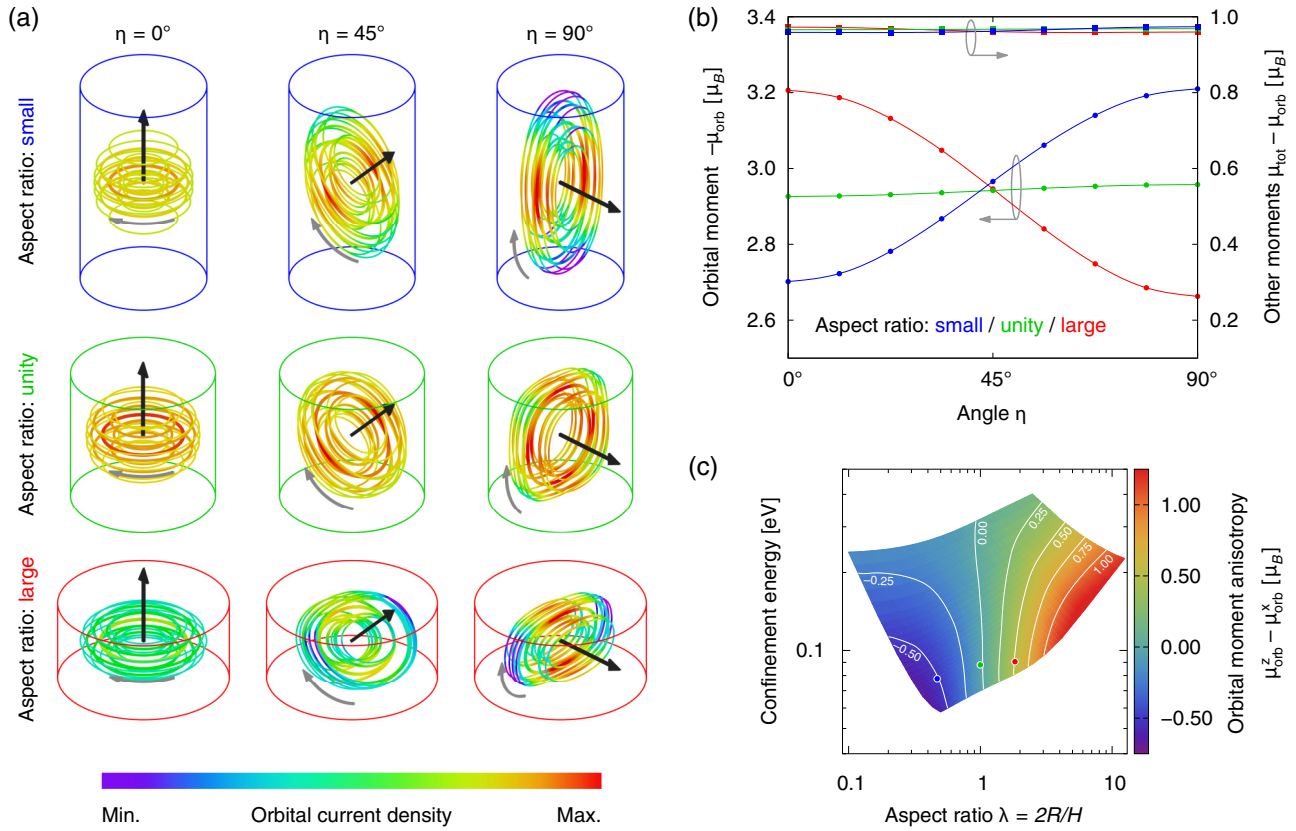

FIG. 1. (a) Selected streamlines of the (itinerant Bloch-velocity-related) orbital current density of the electron ground state of three different cylindrical InAs/InP quantum dots for three different angles η. The current circulates (gray arrow) in a plane perpendicular to the orbital moment (black arrow). (b) The orbital moment for the three quantum dots of (a) as a function of the polar angle η. The pronounced anisotropy is only present for the orbital moment, not for the other contributions to the total magnetic moment. (c) The orbital moment anisotropy depends strongly on the aspect ratio λ and relatively weakly on the confinement energy, from which it is inferred that the anisotropy is governed mainly by the shape of the nanostructure. The three colored dots indicate the three quantum dots shown in (a) and (b).

we summarize here for reference some of our previous findings [24]. These quantum dots were grown by metalorganic vapor-phase epitaxy, resulting in an inhomogeneous size distribution and a broad emission energy range. The ensemble photoluminescence spectrum contained multiple peaks, which we interpreted as a multimodal height distribution. This implied that the emission energy of these quantum dots is strongly correlated with their height. We have measured the heights of more than 50 dots using cross-sectional scanning tunneling microscopy (X-STM) to independently verify this interpretation. The resulting distribution showed that the heights vary between 5 and 15 monolayers (ML) (1.5–4.5 nm), matching well with the peaks found in the ensemble photoluminescence. The X-STM measurements also revealed that the quantum dots resemble cylindrical disks. The lateral size of the quantum dots was found to be less well defined; the largest radius measured 15 nm. These quantum dots have therefore a large aspect ratio and provide a good test ground for our predicted electron g-tensor anisotropy.

The g tensor $\mathbf{g}$ of our quantum dots is diagonal due to their approximate D_{2d} symmetry. We can relate the g factors appearing on the diagonal of the g tensor to the orbital moment via $g^{x,y,z} = 2/\mu_B(\mu_{\text{spin}}^{x,y,z} + \mu_{\text{orb}}^{x,y,z})$. Here $\mu_{\text{spin}}^{x,y,z}$ is the spin moment, $\mu_{\text{orb}}^{x,y,z}$ is the orbital moment, and μ_B is the Bohr magneton. We note that this relation can be derived using the Zeeman interaction and time-reversal symmetry; the factor 2 arises from Kramer's degeneracy. It has been shown [20] that μ_{spin}^{z} is nearly always equal to μ_B. In Fig. 1(b) we have also shown that the spin moment does not exhibit any significant anisotropy. It is therefore a good approximation to set $\mu_{\text{spin}}^{x,y,z} = \mu_B$. Measuring a g factor, therefore, determines effectively the orbital moment in that direction.

A. Experimental methods

The electron and hole ground states of our quantum dots are doubly degenerate at zero magnetic field due to their approximate D_{2d} symmetry (neglecting Coulomb and exchange effects) [21]. A magnetic field lifts this spin degeneracy, which results in four possible optical transitions between the eigenstates of the Zeeman Hamiltonian [42]. Both the electron and hole spin can be effectively described [43] as a spin, $s_{e,h} = \frac{1}{2}$, since the hole state has a strong heavy-hole (HH) character due to quantum confinement and strain [16]. The Zeeman Hamiltonian has then the same form for the electron (e) and hole (h),

$$\mathcal{H}_{\text{Zeeman}}^{e,h} = \mu_B \mathbf{B} \cdot \mathbf{g}_{e,h} \cdot \mathbf{s}_{e,h} = \tfrac{1}{2}\mu_B B \begin{pmatrix} g_{e,h}^{z}\cos\eta & g_{e,h}^{x}\sin\eta \\ g_{e,h}^{x}\sin\eta & -g_{e,h}^{z}\cos\eta \end{pmatrix}, \quad (1)$$

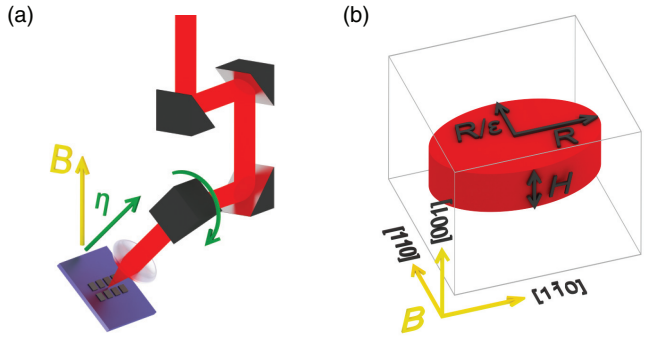

FIG. 2. (a) An *ex situ* rotatable periscope has been used to change the angle η between the magnetic field (yellow) and the sample's normal (green). (b) Calculations have been performed on InAs cylindrical disks (red) embedded in InP with radius R and height H; for some calculations, the radius in the [110] direction is compressed by ϵ; magnetic fields have been applied in the indicated directions.

where $\mathbf{s}_{e,h} = \frac{1}{2}(\sigma_x,\sigma_y,\sigma_z)$ is the spin operator, $\mathbf{B} = (B\sin\eta, 0, B\cos\eta)$ is the magnetic field as defined in Fig. 2(a), and $\mathbf{g}_{e,h}$ is the g tensor. Since light-matter interaction conserves spin, it follows from Eq. (1) that for $\eta = 0°$ (Faraday geometry) only two of the four transitions are optically addressable, from which only $g_e^z + g_h^z$ can be determined. All four transitions are visible when $\eta \neq 0°$. A measurement at $\eta = 90°$ (Voigt geometry) determines separately g_e^x and g_h^x. To separate g_e^z and g_h^z, it is customary [30,31,42] to do an additional measurement at an intermediate angle ($\eta = 45°$).

Following this approach, we have investigated the photoluminescence as a function of a magnetic field up to 10 T at 4 K of 55 individual quantum dots in the same sample used in Ref. [24]. We used a small periscope arrangement of four right-angle mirrors to vary the angle η; see Fig. 2(a). We have used an Al mask with apertures in order to systematically relocate the same quantum dot after changing η *ex situ*. Photoexcitation is provided by a cw 635 nm laser diode; the photoluminescence is collected in backscattering geometry and analyzed using a single grating spectrometer and liquid-nitrogen-cooled InGaAs linear array detector. The spectra are fitted to obtain the peak positions of an individual quantum dot with an accuracy of less than 50 μeV.

In Fig. 3(a), we show the magnetoluminescence of an individual quantum dot up to 10 T for $\eta = (0°, 45°, 90°)$. The polarization of the luminescence is determined at 10 T and is found to be circular ($\sigma^{\pm}$) for $\eta = 0°$ and linear ($\pi_{x,y}$) for $\eta = 90°$. From the fitted peak positions, we obtain the Zeeman energy; see Fig. 3(b). The g tensor can be extracted from these Zeeman energies by fitting them with the transition energies [which follow from diagonalization of Eq. (1)]:

$$E^{\xi_e,\xi_h} = E_0 + \mu_B\Big[\xi_e\sqrt{\left(g_e^x\sin\eta\right)^2 + \left(g_e^z\cos\eta\right)^2} + \xi_h\sqrt{\left(g_h^x\sin\eta\right)^2 + \left(g_h^z\cos\eta\right)^2}\Big]|B| + (\alpha^z\cos^2\eta + \alpha^x\sin^2\eta)B^2, \quad (2)$$

where $\xi_{e,h} = (+,-)$ depending on the electron or hole spin orientation, and E_0 is the transition energy at zero magnetic field. We added the η dependence of the diamagnetic shift using the diamagnetic coefficients at $\eta = 0°$ (α^z) and $\eta = 90°$ (α^x). The Zeeman energies at all values of η are fitted simultaneously with Eq. (2); see Figs. 3(b) and 3(c). Using this procedure, we have extracted the g factors and diamagnetic coefficients for 55 individual quantum dots having different emission energies E_0, which we will discuss in Secs. III B–III D. We refer the reader to the Appendix for a detailed discussion on the assumptions made in the fitting procedure; these influence the assignment and sign of the various g factors.

To understand the origin and size dependence of the experimentally measured g factors in detail, we calculated the g factors using the same $\mathbf{k}\cdot\mathbf{p}$ model used in Sec. II. The quantum dots are modeled as pure InAs disks embedded in InP; see Fig. 2(b). The separate electron and hole energy levels of a quantum dot have been calculated as a function of a magnetic field applied in the growth [001] direction or in-plane ⟨110⟩ directions. We can then directly extract from these energy levels the Zeeman energy ($g_{e,h}^{x,z}$ factors) and diamagnetic shift ($\alpha_{e,h}^{x,z}$). Both the size of the quantum dot and elongation of its footprint, $\varepsilon = R_{[1\bar{1}0]}/R_{[110]}$, have been varied. We have left out the remote-band coupling of the hole spin to the magnetic field in all calculations, as previous work indicated that this is a better approximation than including them [16].

B. Electron g factors

From Fig. 4, we see that the measured electron g factors are strongly correlated with the emission energy. As the emission energy is strongly determined by the height of the quantum dots [24], these trends can therefore be interpreted as the height dependence of the g factor. A comparison between the trends of the experimental data and the calculated electron g factors confirms this conclusion. We simultaneously conclude that all quantum dots have more or less the same radius, which agrees well with the observation that the diamagnetic coefficients do not depend much on the emission energy (see Sec. III D). A radius between 7 and 11 nm and a height between 1.8 and 6.0 nm gives the best match between experiment and calculations. This agrees well with the average height of 3 nm and maximum radius of 15 nm determined by X-STM [24]. We would like to stress that the calculations with the $\mathbf{k}\cdot\mathbf{p}$ model are fit-free and completely independent from the experimental results. We attribute deviations between the experimental and calculated g factors to differences between the real and modeled shape, size, and composition of the quantum dots.

Recently, InAs/$In_{0.53}Al_{0.24}Ga_{0.23}$ quantum dots, which also emit around 800 meV, have been investigated [44]. Although these quantum dots have a confinement energy comparable to our quantum dots, their average size (radius of 25 nm and height of 13 nm) and composition differ substantially. Based on the framework of the orbital currents, we would expect the larger size of the InAs/$In_{0.53}Al_{0.24}Ga_{0.23}$ to result in a larger orbital moment. Indeed, g_e^x was measured to be about -1.9, which is more negative than our measurements. It shows that a g factor is more affected by the size of a quantum dot than by its confinement energy.

A more prominent experimental observation can be made by comparing Figs. 4(a) and 4(b): for each quantum dot, g_e^x is significantly closer to the free-electron value of $+2$ than g_e^z. Translated in terms of the orbital moment: for every

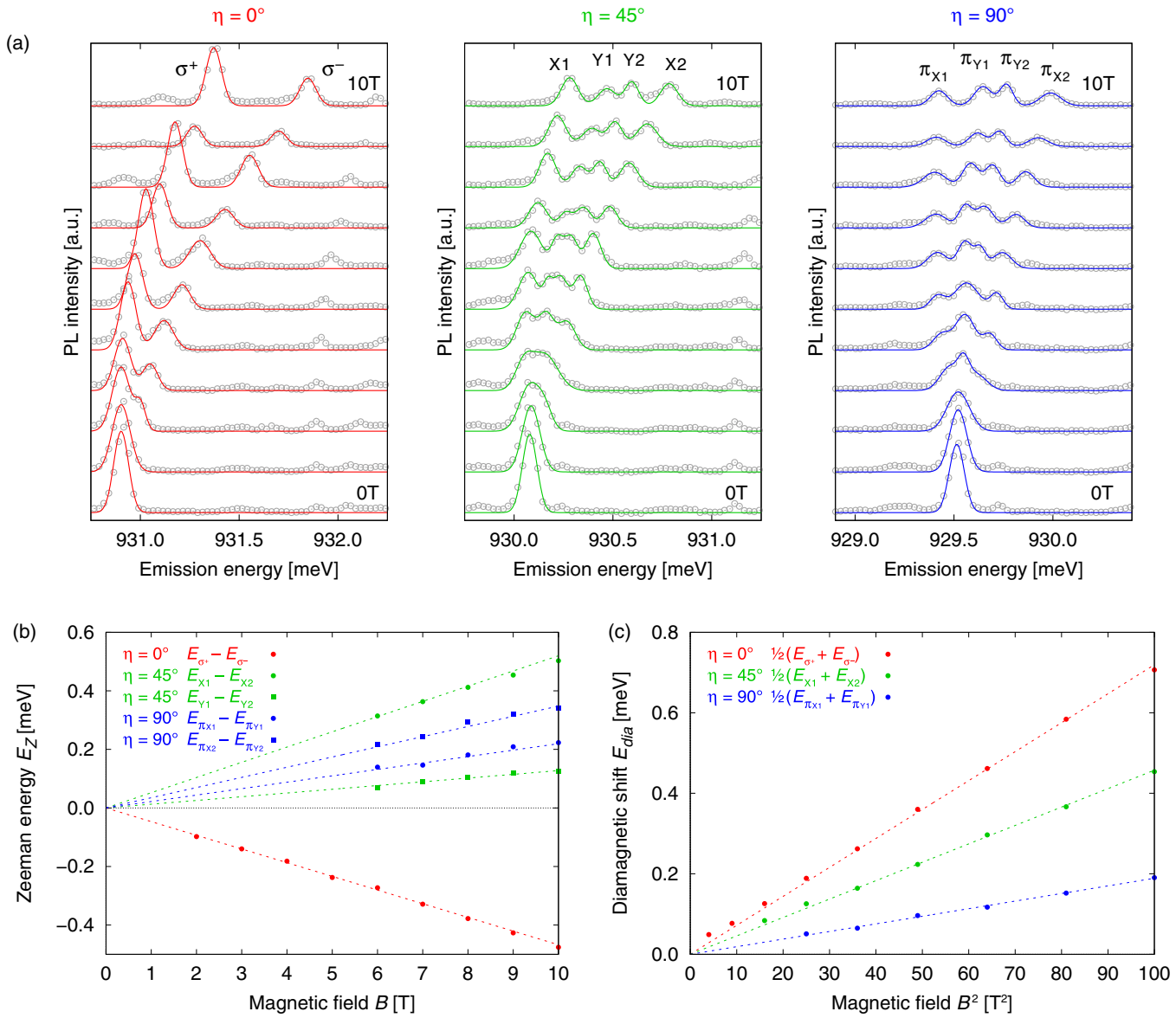

FIG. 3. (a) An example of the magnetoluminescence up to 10 T of a single quantum dot for $\eta = 0°$, 45°, and 90°. The experimental data (gray points) and the fits (colored lines) are offset for clarity for increasing magnetic field. We obtain from the fitted peak positions the Zeeman energies (b) and diamagnetic shifts (c). By simultaneous fitting of these energies using Eq. (2), we find for this particular quantum dot ($g_e^x = 0.60, g_e^z = -0.51, g_h^x = 0.38, g_h^z = -0.29$) and ($\alpha^z = 7.2\ \mu$ eV/T^2,$\alpha^{45°} = 4.6\ \mu$ eV/T^2,$\alpha^x = 1.9\ \mu$ eV/T^2).

quantum dot, we observe $\mu^x_{\rm orb} < \mu^z_{\rm orb}$. This complies with our theoretical prediction: as these cylindrical quantum dots have a large aspect ratio, the orbital current can encircle a much larger area when the orbital moment is along the symmetry axis than when it is directed in-plane. Although the anisotropy of the electron g factor has been measured experimentally in quantum wells [45] and quantum dots [29–31,35–37], the reported anisotropies have been generally small and were not explained using this simple geometrical argument. We point out that the anisotropy makes it possible to size-engineer separately g_e^x and g_e^z close to zero, where an additional electric field can then be used to change the sign of the g factor.

The behavior of electron g tensors is sometimes explained using "averaging methods": the penetration of the state into the barriers determines, through the difference of the bulk g factors of the nanostructure and barrier material, the value of the g factor. Interestingly, the averaging method would predict an isotropic electron g tensor, since the penetration into the barrier material is independent of the spin orientation (neglecting the very small anisotropy of the bulk g tensor). Although the shortcomings of this approach have been pointed out before [13,16], our experimentally observed strong anisotropy of the electron g tensor invalidates this type of approach.

The geometrical argument complies well with some details in the size dependence of the calculated g factors. First, we observe in Fig. 4 that for a fixed height, the radius has a much larger influence on g_e^z (sensitive to R^2) than on g_e^x (sensitive to $RH/2$). In particular, we see that for very flat quantum dots, the radius has very little influence on g_e^x and affects only the emission energy. Secondly, we see that elongation slightly

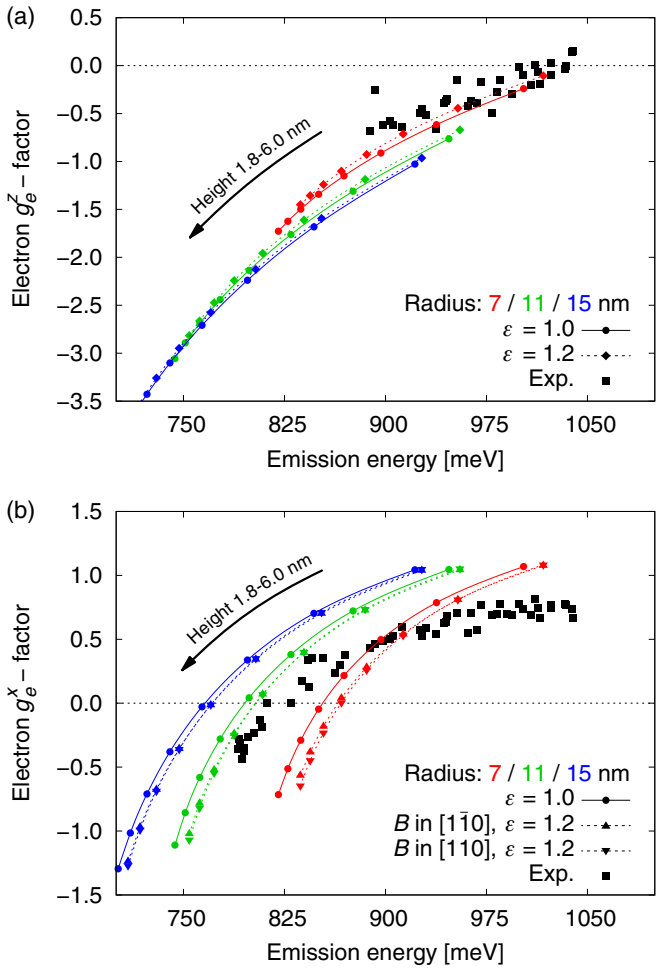

FIG. 4. The experimentally measured (black squares, $\Delta g = 0.1$) and calculated (colored curves) electron g_e^z (a) and g_e^x (b) factors as a function of the emission energy of the quantum dot. The different colors indicate different radii of the disks; the height is varied from 1.8 to 6.0 nm along a curve of fixed radius. The continuous lines represent cylindrical disks, while the dotted curves are for an elongated disk with $\varepsilon = 1.2$. In the latter case, the in-plane orientation of the magnetic field ([110] upward triangles, [1$\bar{1}$0] downward triangles) affects the calculated g_e^x factors.

decreases μ_{orb}^z, since it limits the total area for the current to circulate. Simultaneously, we observe that elongation does not have a great effect on μ_{orb}^x, as the area for the current to circulate in is mainly limited by the height. Lastly, we see that μ_{orb}^x is largest if the magnetic field is along the [110] direction, since the area for the current to circulate in is now enlarged by the elongation.

The prominent height dependence of g_e^z cannot be intuitively explained using the geometrical argument. This dependence is therefore related to the size dependence of the integrated current [20]. For the small heights considered here, the integrated current gets smaller with decreasing height: the valence-band contributions to the electron ground state are quenched through their dependence on the confinement energy. This explains why the calculated curves for different radii are more or less falling on top of each other: g_e^z is mainly parametrized by the confinement energy. The confinement energy scales with the volume of the quantum dot for a fixed aspect ratio. The g_e^z factor depends, therefore, mostly on the volume, as was found before [13].

C. Hole *g* factors

From Figs. 5(a) and 5(b), we observe that the experimentally found g_h^x and g_h^z are very different: the hole g tensor is even more anisotropic than the electron g tensor. Contrary to the electrons, the strong (weak) correlation of g_h^z (g_h^x) with emission energy makes it possible to size-engineer the hole g tensor to become isotropic. Moreover, the sign of the g_h^z factors changes around 900 meV, which can be beneficial for applications.

To explain this behavior, we need to trace the origin of the orbital moment of the hole ground state. As a first approximation, the hole state is a pure HH state. Such a state has, in addition to its spin moment, only a localized Bloch orbital moment that is projected along the z axis: we would therefore expect $g_h^x = 0$ and $g_h^z = +4$. From Figs. 5(a) and 5(b) we see that this expectation is not far off for g_h^x, but both the experimental and calculated g_h^z behave very differently. This points to the more complicated nature of the hole orbital moment compared to the electron orbital moment. In general, contributions from other bands lead to additional localized and itinerant orbital currents. For the electron state, it turns out that the itinerant current dominates all other contributions [19], such that it solemnly explains the experimentally observed trends as we have shown in Sec. III B. For the hole state, however, both types of currents contribute equally, thereby complicating the analysis.

To make progress, we can semiquantitatively investigate the first and most important contribution to the hole state: the light-hole (LH) band. In Fig. 5(c), we show the LH contribution of the calculated hole ground state for the same sizes of quantum dots as in Figs. 5(a) and 5(b). We observe that the LH contribution increases with increasing height, decreasing radius, and increasing elongation. This behavior can be understood by inspecting the part of the eight-band Hamiltonian describing the Γ_8^v bands [46]:

$$\mathcal{H}_{\Gamma_8^v} = \begin{pmatrix} E_{\text{HH}} & L & M & 0 \\ L^* & E_{\text{LH}} & 0 & M \\ M^* & 0 & E_{\text{LH}} & -L \\ 0 & M^* & -L^* & E_{\text{HH}} \end{pmatrix}, \tag{3}$$

where

$$E_{\text{HH}} = -\frac{\hbar^2\left(k_x^2 + k_y^2\right)}{2m_0}(\gamma_1 + \gamma_2) - \frac{\hbar^2 k_z^2}{2m_0}(\gamma_1 - 2\gamma_2), \tag{4}$$

$$E_{\text{LH}} = -\frac{\hbar^2\left(k_x^2 + k_y^2\right)}{2m_0}(\gamma_1 - \gamma_2) - \frac{\hbar^2 k_z^2}{2m_0}(\gamma_1 + 2\gamma_2), \tag{5}$$

$$L = \sqrt{3}\frac{\hbar^2(k_x - ik_y)k_z}{m_0}\gamma_3, \tag{6}$$

$$M = \sqrt{3}\frac{\hbar^2(k_x - ik_y)^2}{2m_0}\gamma_3, \tag{7}$$

where $k_{x,y} \sim 1/R$ and $k_z \sim 1/H$ are the wave numbers of the state [47], and $\gamma_{1,2,3}$ are the Luttinger parameters. In

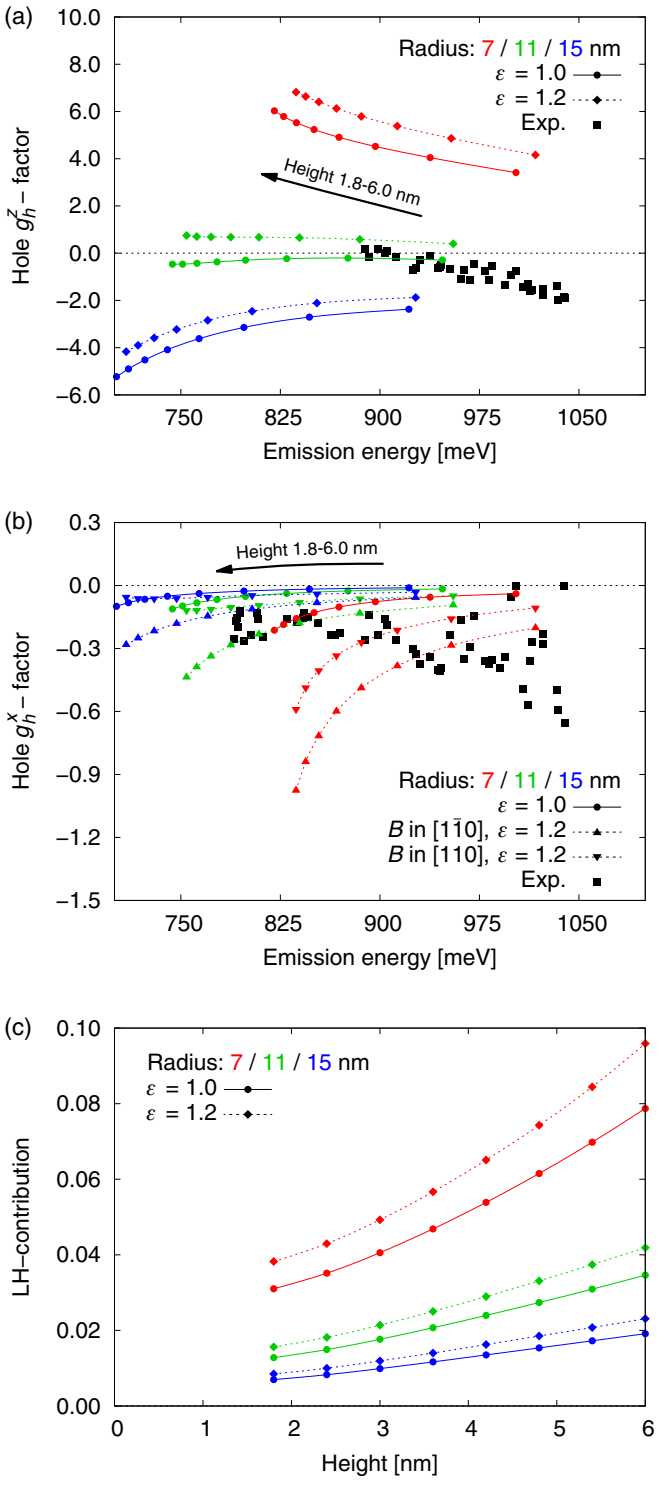

FIG. 5. The experimentally measured (black squares, $\Delta g = 0.1$) and calculated (colored curves) hole g_h^z (a) and g_h^x (b) factors as a function of the emission energy of the quantum dot. The different colors indicate different radii of the disks; the height is varied from 1.8 to 6.0 nm along a curve of fixed radius. The continuous lines represent cylindrical disks, while the dotted curves are for an elongated disk with $\varepsilon = 1.2$. In the latter case, the in-plane orientation of the magnetic field ([110] upward triangles, [1$\bar{1}$0] downward triangles) affects the calculated g_h^x factors. (c) The LH contribution to the calculated hole ground state for different heights and radii of the quantum dots.

the framework of perturbation theory, the amount of LH contribution in the hole state is proportional to the coupling between the HH and LH bands (matrix elements L and M) divided by the energetic splitting between the bands ($E_{\mathrm{HH}} - E_{\mathrm{LH}}$). As for our quantum dots $H \ll R$, we immediately infer that the hole state is predominantly HH in character. Moreover, we see that upon increasing the height (radius), the energetic splitting $E_{\mathrm{HH}} - E_{\mathrm{LH}}$ becomes smaller (larger) and hence the LH contribution becomes larger (smaller), as we observe in Fig. 5(c). Also, the increase of the LH contribution with elongation can be explained, since the coupling terms L and M are proportional to $k_x - k_y \propto \varepsilon$.

Comparing Figs. 5(b) and 5(c), we observe a positive correlation between the LH contribution and the magnitude of the calculated g_h^x factors. Elongation also increases the calculated g_h^x and has a more profound influence than the LH contribution, pointing out that elongation affects g_h^x also via other bands. The large spread of the measured g_h^x at high emission energy can therefore be attributed to a larger LH contribution or elongation. In previous experiments, we found about 20% of our quantum dots to exhibit an anisotropic exchange splitting at zero magnetic field [24]. Since this splitting increased toward higher emission energies, we tentatively argued that the elongation is more pronounced at higher emission energies. Such an effect could explain the experimentally observed increase of g_h^x at large emission energies.

Both the measured and calculated g_h^z show a clear trend with emission energy. The calculated g_h^z also depends strongly on the radius, which could be related to the area ($\propto R^2$) in which the itinerant orbital current circulates. Also, the integrated current I itself might depend directly on the radius through the size dependence of the contributions of other bands. The combined effect might explain the unexpected strong radius dependence of the calculated g_h^z factors. We again point out that the localized orbital currents might also play a significant role here.

D. Diamagnetic coefficients

An external magnetic field induces through the Lorentz force an orbital current for carriers confined in quantum dots, analogous to Langevin diamagnetism in atoms. In contrast to the spin-correlated currents underlying the g tensor, this magnetic-field-induced current is spin-independent. For a magnetic field along the z axis, an elementary derivation shows that this leads to a diamagnetic shift in energy,

$$\mu_{\mathrm{dia}} = IA = \left(\frac{-e\omega}{2\pi}\right)\pi R^2 \rightarrow E_{\mathrm{dia}} = -\mu_{\mathrm{dia}} B = \frac{e^2 R^2}{4m^*} B^2, \tag{8}$$

where $\omega = eB/2m^*$ due to Larmor precession, and m^* is the effective mass. The factor in front of the B^2 dependence is defined as the diamagnetic coefficient α. In analogy with the spin-correlated currents (Sec. II), we therefore intuitively expect

$$\alpha^z \propto \frac{R^2}{m_z^*(R,H)}, \quad \alpha^x \propto \frac{RH}{m_x^*(R,H)}. \tag{9}$$

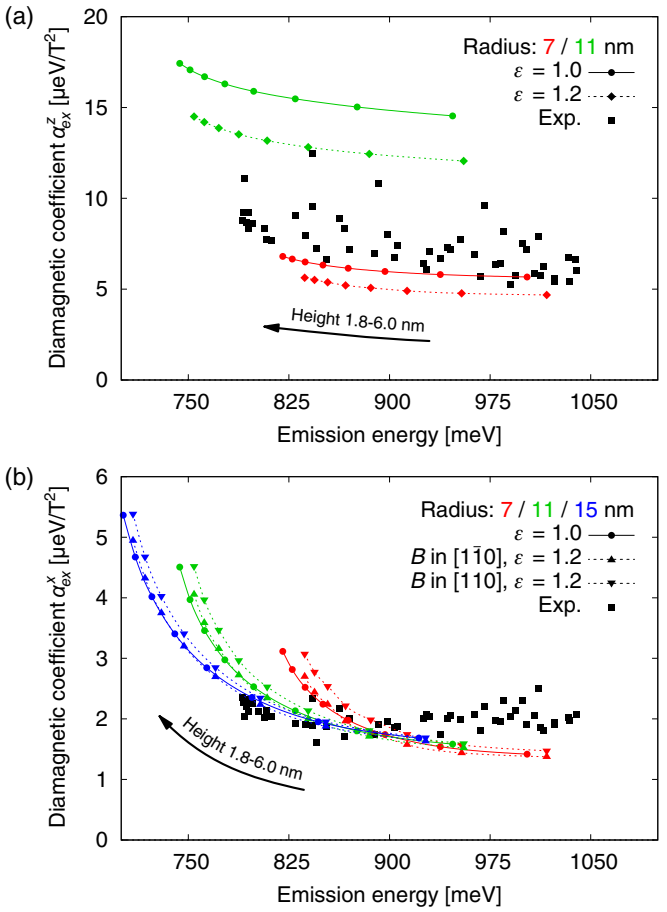

FIG. 6. The experimentally measured (black squares) and calculated (coloured curves) exciton diamagnetic coefficients α_{ex}^z (a) and α_{ex}^x (b) as a function of the emission energy of the quantum dot. The different colors indicate different radii of the disks; the height is varied from 1.8 to 6.0 nm along a curve of fixed radius. The continuous lines represent cylindrical disks, while the dotted curves are for an elongated disk with $\varepsilon = 1.2$. In the latter case, the in-plane orientation of the magnetic field ([110] upward triangles, [1$\bar{1}$0] downward triangles) affects the calculated diamagnetic coefficients.

Similar to the anisotropy of the electron g tensor, the diamagnetic energy anisotropy is sensitive to the shape of the quantum dot through the area encircled by the magnetic-field-induced current. Note that it also depends, through effective-mass anisotropy, on the size of the quantum dots.

Experimentally, we measure the exciton diamagnetic coefficients α_{ex}, which contain the combined electron and hole diamagnetic coefficients. We still expect that the anisotropy of α_{ex} is largely determined by the aspect ratio, since the hole effective mass is much larger than the electron effective mass. It is therefore possible to approximately infer from the anisotropy of α_{ex} what aspect ratio the nanostructures have. We find from the measurements shown in Fig. 6 that $\alpha_{ex}^z/\alpha_{ex}^x = (3.7 \pm 0.9)$, meaning that our quantum dots are indeed flat disks. Moreover, the ratio's weak dependence on the emission energy indicates that all quantum dots have a similar aspect ratio. This independently validates the results of the structural analysis [24] and the assertions made in the discussion on the g tensors.

The α_{ex}^z [see Fig. 6(a)] are similar to the previously reported exciton diamagnetic coefficients [24]. The weak dependence on the emission energy indicates that the measured quantum dots have similar radii. This complies well with the comparison between the measured and calculated electron g factors: also, we found there that a single radius gives the best match. We find again that a radius between 7 and 11 nm gives the best match between experiment and calculations; this can be improved further by including Coulomb corrections [16]. As expected, the theoretically calculated α_{ex}^z depend strongly on the radius and the elongation, as both influence the area the magnetic-field-induced orbital current circulates. Their less intuitive height dependence was previously found to be related to the size (or energy) dependence of the effective mass [16].

The α_{ex}^x [see Fig. 6(b)] has not been previously measured systematically at different emission energies. There is good agreement between the experimentally observed and calculated α_{ex}^x; the deviation at larger emission energies could be related to the discrepancy found for the g_h^x factors at those energies. The calculated α_{ex}^x depend relatively more strongly on the height than the α_{ex}^z: this complies with our expectation that α_{ex}^x is directly proportional to the height. Indeed, we find from our calculations that the separate electron and hole diamagnetic coefficients are (approximately) linearly dependent on both height and radius (not shown here).

IV. CONCLUSIONS

We have predicted that the anisotropy of the electron g tensor is strongly correlated with the shape of the nanostructure in a fashion traceable to the behavior of the spin-correlated orbital currents. The orbital current that generates the spin-correlated electron orbital moment circulates in a plane perpendicular to the moment's orientation. The resulting simple current loop is therefore sensitive to the shape of the nanostructure. For cylindrical quantum dots, this results in the anisotropic electron g tensor, which is governed mainly by the aspect ratio of the quantum dots. Through a systematic study of the size dependence of the separate electron and hole g tensors of flat quantum dots, we have verified that this picture is valid. Moreover, the experimentally observed anisotropy directly invalidates "averaging methods" for calculating g factors.

We find that through size-engineering it is possible to independently change the sign of the in-plane and growth direction electron g factors. The influence of elongation follows the intuitive picture of the simple current loop, and it is of small influence for the electron g tensor. The hole g tensor is strongly anisotropic and very sensitive to the radius and elongation. Although the underlying hole orbital moment can be partially understood from the LH contribution, the equal importance of both itinerant and localized currents complicates the analysis over the electron case.

The approximate analogous role of circulating currents on the diamagnetic coefficients and g tensors means that the shape of the nanostructures also determines the anisotropy of the diamagnetic coefficients. It is therefore possible to infer from the anisotropy of the diamagnetic coefficients what aspect ratio the nanostructures have.

ACKNOWLEDGMENTS

M.E.F. acknowledges support from an AFOSR MURI. J.v.B., A.Yu.S., and P.M.K. acknowledge support by the COBRA Research Institute.

APPENDIX: COMMENTS ON ASSIGNMENT, SIGN, AND DETECTION RANGE OF g FACTORS

As can be seen from Eq. (2), only the absolute value of the g factors is relevant for determining the energy levels in the $\eta = 45^\circ$ geometry. Therefore, the sign of $g^z_{e,h}$ ($g^x_{e,h}$) is determined solely by the $\eta = 0^\circ$ ($\eta = 90^\circ$) measurements. In the Faraday measurements, the circular polarization state of light leads directly to the sign of the exciton g^z_{ex} factor:

$$g^z_{\rm ex} = \frac{E_{\sigma^+} - E_{\sigma^-}}{\mu_B B} = g^z_e + g^z_h, \tag{A1}$$

which complies with the usual definitions [14,24]. As in our measurements, $g^z_{\rm ex} \neq 0$, this relation determines directly the sign of the separate electron and hole g^z factors.

The situation is more complicated for the Voigt measurements, as it is neither possible to assign the measured g factors to a specific carrier, nor to establish their sign: it is *a priori* not clear which of the two linearly polarized Zeeman splittings belongs to which transition. It has been shown for quantum wells [48] and ensembles of quantum dots [49] that the in-plane orientation of the linear polarization axis depends on the relative in-plane orientation of the electron and hole spin. Details of the hole state, such as light-hole intermixing and the nonlinear remote-band coupling of the magnetic field to the hole spin, can lead to the peculiar situation in which the in-plane orientation of the polarization axis depends nontrivially on the in-plane magnetic-field orientation [49]. Only by measuring this dependence would it be possible to attribute the Zeeman splittings to a certain carrier.

In Fig. 7 we show that this situation also applies to our quantum dots: we use the $\mathbf{k}\cdot\mathbf{p}$ model to calculate the in-plane orientation of the linear polarization axis of the ground-state dipole transitions for various in-plane orientations of the magnetic field. We note that these effects are virtually absent when the quantum dot is elongated: the polarization axis is relatively unaffected by the in-plane orientation of the magnetic field. Since we have no clear experimental evidence for such elongation in our quantum dots, we opted pragmatically to rely on the simultaneous fit of the $\eta = 45^\circ$ and 90° data, where the goodness of the fit depends on the assignment of the Zeeman energies to a certain carrier.

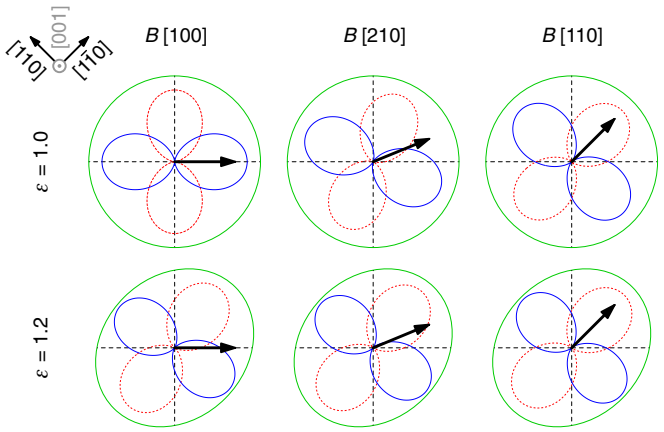

FIG. 7. The calculated linear polarization pattern (blue/red) for emission along the z axis when the in-plane magnetic field is rotated from the [100] direction toward the [110] direction of a quantum dot with a radius of 11 nm and height of 2.4 nm. In the absence of elongation (top row), there is an intricate dependence of the emission pattern on the orientation of the magnetic field, which is absent when the quantum dot's footprint (green) is compressed in the [110] direction (bottom row).

The sign of the $g^x_{e,h}$ factors cannot be determined directly from the measurements. The inner two peaks of all quantum dots emitting at energies $\gtrsim$825 meV are y-polarized; see, for example, Fig. 3(a). However, the inner peaks are x-polarized for quantum dots emitting $\lesssim$825 meV, from which we infer that the relative sign between g^x_e and g^x_h changes. The measured g^x_e factor is zero around these energies; see Fig. 4(b). Since we expect g^x_e to tend to the free-electron g factor of $+2$ at high emission energy [13] (small quantum dots) and to the strained bulk InAs electron g factor of about -5 at low emission energy [50] (large quantum dots), we *choose* $g^x_e > 0$ for emission energies $>$825 meV. The sign of g^x_h follows then automatically.

We have found that two of the four peaks below 850 meV in the $\eta = 45^\circ$ measurements dropped significantly in intensity. Lacking those two peaks, it was not possible to separate the electron and hole g factor for the Faraday measurements below 850 meV. Using the eigenstates of the Hamiltonian in Eq. (1), we have calculated the emission intensity of the peaks for $\eta = 45^\circ$. As the intensity depends on the g factors, we used the measured g factors to parametrize the intensity as a function of the emission energy. We then found indeed that the emission intensity of two of the four peaks drops sharply below 850 meV, due to accidental numerical values of the g factors. We predict that below 700 meV these two peaks have sufficient intensity to be measured, although this is outside the detection range of the InGaAs detector. Note that the Voigt measurements do span the full detection range.

[1] D. Loss and D. P. DiVincenzo, Phys. Rev. A **57**, 120 (1998).

[2] B. E. Kane, Nature (London) **393**, 133 (1998).

[3] Y. Kato, R. C. Myers, A. C. Gossard, J. Levy, and D. D. Awschalom, Science **299**, 1201 (2003).

[4] J. Pingenot, C. E. Pryor, and M. E. Flatté, Appl. Phys. Lett. **92**, 222502 (2008).

[5] T. Andlauer and P. Vogl, Phys. Rev. B **79**, 045307 (2009).

[6] A. De, C. E. Pryor, and M. E. Flatté, Phys. Rev. Lett. **102**, 017603 (2009).

[7] J. Pingenot, C. E. Pryor, and M. E. Flatté, Phys. Rev. B **84**, 195403 (2011).

[8] G. Salis, Y. Kato, K. Ensslin, D. C. Driscoll, A. C. Gossard, and D. D. Awschalom, Nature (London) **414**, 619 (2001).

[9] R. Hanson, L. P. Kouwenhoven, J. R. Petta, S. Tarucha, and L. M. K. Vandersypen, Rev. Mod. Phys. **79**, 1217 (2007).

[10] R. J. Warburton, Nat. Mater. **12**, 483 (2013).

[11] J. Houel, J. H. Prechtel, A. V. Kuhlmann, D. Brunner, C. E. Kuklewicz, B. D. Gerardot, N. G. Stoltz, P. M. Petroff, and R. J. Warburton, Phys. Rev. Lett. **112**, 107401 (2014).

[12] A. A. Kiselev, E. L. Ivchenko, and U. Rössler, Phys. Rev. B **58**, 16353 (1998).

[13] C. E. Pryor and M. E. Flatté, Phys. Rev. Lett. **96**, 026804 (2006).

[14] C. E. Pryor and M. E. Flatté, Phys. Rev. Lett. **99**, 179901(E) (2007).

[15] T. Andlauer, R. Morschl, and P. Vogl, Phys. Rev. B **78**, 075317 (2008).

[16] J. van Bree, A. Y. Silov, P. M. Koenraad, M. E. Flatté, and C. E. Pryor, Phys. Rev. B **85**, 165323 (2012).

[17] R. Zielke, F. Maier, and D. Loss, Phys. Rev. B **89**, 115438 (2014).

[18] Y. Yafet, Solid State Phys. **14**, 1 (1963).

[19] J. van Bree, A. Y. Silov, P. M. Koenraad, and M. E. Flatté, Phys. Rev. Lett. **112**, 187201 (2014).

[20] J. van Bree, A. Y. Silov, P. M. Koenraad, and M. E. Flatté, Phys. Rev. B **90**, 165306 (2014).

[21] M. Bayer, G. Ortner, O. Stern, A. Kuther, A. A. Gorbunov, A. Forchel, P. Hawrylak, S. Fafard, K. Hinzer, T. L. Reinecke, S. N. Walck, J. P. Reithmaier, F. Klopf, and F. Schäfer, Phys. Rev. B **65**, 195315 (2002).

[22] T. Nakaoka, T. Saito, J. Tatebayashi, and Y. Arakawa, Phys. Rev. B **70**, 235337 (2004).

[23] D. Kim, W. Sheng, P. J. Poole, D. Dalacu, J. Lefebvre, J. Lapointe, M. E. Reimer, G. C. Aers, and R. L. Williams, Phys. Rev. B **79**, 045310 (2009).

[24] N. A. J. M. Kleemans, J. van Bree, M. Bozkurt, P. J. van Veldhoven, P. A. Nouwens, R. Nötzel, A. Y. Silov, P. M. Koenraad, and M. E. Flatté, Phys. Rev. B **79**, 045311 (2009).

[25] V. Jovanov, T. Eissfeller, S. Kapfinger, E. C. Clark, F. Klotz, M. Bichler, J. G. Keizer, P. M. Koenraad, G. Abstreiter, and J. J. Finley, Phys. Rev. B **83**, 161303 (2011).

[26] V. Jovanov, T. Eissfeller, S. Kapfinger, E. C. Clark, F. Klotz, M. Bichler, J. G. Keizer, P. M. Koenraad, M. S. Brandt, G. Abstreiter, and J. J. Finley, Phys. Rev. B **85**, 165433 (2012).

[27] M. Bayer, A. Kuther, A. Forchel, A. Gorbunov, V. B. Timofeev, F. Schäfer, J. P. Reithmaier, T. L. Reinecke, and S. N. Walck, Phys. Rev. Lett. **82**, 1748 (1999).

[28] A. Högele, M. Kroner, S. Seidl, K. Karrai, M. Atatüre, J. Dreiser, A. Imamoglu, R. J. Warburton, A. Badolato, B. D. Gerardot, and P. M. Petroff, Appl. Phys. Lett. **86**, 221905 (2005).

[29] T. Nakaoka, S. Tarucha, and Y. Arakawa, Phys. Rev. B **76**, 041301 (2007).

[30] T. Kehoe, M. Ediger, R. T. Phillips, and M. Hopkinson, Rev. Sci. Instrum. **81**, 013906 (2010).

[31] B. J. Witek, R. W. Heeres, U. Perinetti, E. P. A. M. Bakkers, L. P. Kouwenhoven, and V. Zwiller, Phys. Rev. B **84**, 195305 (2011).

[32] A. Schwan, B.-M. Meiners, A. Greilich, D. R. Yakovlev, M. Bayer, A. D. B. Maia, A. A. Quivy, and A. B. Henriques, Appl. Phys. Lett. **99**, 221914 (2011).

[33] R. S. Deacon, Y. Kanai, S. Takahashi, A. Oiwa, K. Yoshida, K. Shibata, K. Hirakawa, Y. Tokura, and S. Tarucha, Phys. Rev. B **84**, 041302 (2011).

[34] T. M. Godden, J. H. Quilter, A. J. Ramsay, Y. Wu, P. Brereton, I. J. Luxmoore, J. Puebla, A. M. Fox, and M. S. Skolnick, Phys. Rev. B **85**, 155310 (2012).

[35] A. J. Bennett, M. A. Pooley, Y. Cao, N. Sköld, I. Farrer, D. A. Ritchie, and A. J. Shields, Nat. Commun. **4**, 1522 (2013).

[36] J. H. Prechtel, F. Maier, J. Houel, A. V. Kuhlmann, A. Ludwig, A. D. Wieck, D. Loss, and R. J. Warburton, Phys. Rev. B **91**, 165304 (2015).

[37] S. Takahashi, R. S. Deacon, A. Oiwa, K. Shibata, K. Hirakawa, and S. Tarucha, Phys. Rev. B **87**, 161302 (2013).

[38] C. Pryor, Phys. Rev. B **57**, 7190 (1998).

[39] K. Gündoğdu, K. C. Hall, E. J. Koerperick, C. E. Pryor, M. E. Flatté, T. F. Boggess, O. B. Shchekin, and D. G. Deppe, Appl. Phys. Lett. **86**, 113111 (2005).

[40] M. Montazeri, M. Fickenscher, L. M. Smith, H. E. Jackson, J. Yarrison-Rice, J. H. Kang, Q. Gao, H. H. Tan, C. Jagadish, Y. Guo, J. Zou, M.-E. Pistol, and C. E. Pryor, Nano Lett. **10**, 880 (2010).

[41] I. Vurgaftman, J. R. Meyer, and L. R. Ram-Mohan, J. Appl. Phys. **89**, 5815 (2001).

[42] D. Gammon, A. Efros, J. Tischler, A. Bracker, V. Korenev, and I. Merkulov, in *Quantum Coherence Correlation and Decoherence in Semiconductor Nanostructures*, edited by T. Takagahara (Academic, San Diego, 2003), pp. 207–280.

[43] H. W. van Kesteren, E. C. Cosman, W. A. J. A. van der Poel, and C. T. Foxon, Phys. Rev. B **41**, 5283 (1990).

[44] V. V. Belykh, A. Greilich, D. R. Yakovlev, M. Yacob, J. P. Reithmaier, M. Benyoucef, and M. Bayer, Phys. Rev. B **92**, 165307 (2015).

[45] R. Winkler, *Spin-orbit Coupling Effects in Two-Dimensional Electron and Hole Systems* (Springer, Berlin, 2003).

[46] T. B. Bahder, Phys. Rev. B **41**, 11992 (1990).

[47] F. V. Kyrychenko and J. Kossut, Phys. Rev. B **70**, 205317 (2004).

[48] Y. G. Kusrayev, A. V. Koudinov, I. G. Aksyanov, B. P. Zakharchenya, T. Wojtowicz, G. Karczewski, and J. Kossut, Phys. Rev. Lett. **82**, 3176 (1999).

[49] T. Kiessling, A. V. Platonov, G. V. Astakhov, T. Slobodskyy, S. Mahapatra, W. Ossau, G. Schmidt, K. Brunner, and L. W. Molenkamp, Phys. Rev. B **74**, 041301 (2006).

[50] G. Hendorfer and J. Schneider, Semicond. Sci. Technol. **6**, 595 (1991).